An Updated Parametrization of Algorithms to Retrieve the Diffuse Attenuation of Light in the Ocean from Remote Sensing and its Impact on Estimates of Net Primary Productivity

Charlotte Begouen Demeaux [1*], Emmanuel Boss[1], and Toby K. Westberry[2]
[1]School of Marine Sciences, University of Maine, 360 Aubert Hall, Orono, ME 04469, USA.
[2]Department of Botany and Plant Pathology, Oregon State University, Corvallis, OR, 97331, USA.
*Corresponding author: charlotte.begouen@maine.edu

An Updated Parametrization of Algorithms to Retrieve the Diffuse Attenuation of Light in the Ocean from Remote Sensing and its Impact on Estimates of Net Primary Productivity

Charlotte Begouen Demeaux[1*], Emmanuel Boss[1], and Toby K. Westberry[2]

[1]School of Marine Sciences, University of Maine, 360 Aubert Hall, Orono, ME 04469, USA.

[2]Department of Botany and Plant Pathology, Oregon State University, Corvallis, OR, 97331, USA.

[*]Corresponding author : charlotte.begouen@maine.edu

February 9, 2023

Abstract

We recently found a significant bias while validating frequently used ocean color algorithms retrieving the spectral diffuse attenuation coefficient ($K_d(\lambda)$)[1]. Here we modify existing algorithms for $K_d(\lambda)$ to remove the observed bias at $K_d(490)$, and evaluate the impact on global and regional estimates of net primary production (NPP) using two different primary production models. The new parametrization results in improved retrievals of $K_d(490)$ by all algorithms. The new coefficients are validated using measurements not included in the training dataset and are found to perform significantly better at a different wavelength (412nm) than the one used for the new parametrization (490nm) and perform reasonably well in Case-2 waters. Since the new coefficients were developed with a dataset encompassing larger proportions of the ocean's variability, they are better suited to compute $K_d(\lambda)$ in regions that weren't present in the original algorithm's dataset and are therefore appropriate for global $K_d(\lambda)$ estimation. Using the new K_d parameterization results in a global increase of NPP of $\approx 37\%$, mostly driven by the previous overestimation of $K_d(\lambda)$ (underestimation of light penetration) in the clear, subtropical gyres. Subtropical gyres show the largest increase (79%) in the VGPM model. Their large surface area and the magnitude of the bias in $K_d(\lambda)$ in the old parameterization causes the observed difference in global NPP estimates. Our results suggest that the oceanic carbon uptake is larger than previously thought, which will be most relevant to the oceanic carbon dioxide budget once humanity slows the increase of atmospheric CO_2.

1 Introduction

Accurately retrieving the spectral diffuse attenuation coefficient of downwelling irradiance ($K_d(\lambda)$) from Remote Sensing Reflectance (R_{rs}) estimated with Ocean Color radiometry measured on board satellites is of importance when trying to quantify the penetration of solar radiation from the surface to depth. Diffuse attenuation coefficients (K_ds) are Apparent Optical Properties (AOPs) that convey information on the optical properties of the water while being moderately affected by external environmental conditions impacting the light field (such as solar angle, clouds, passing waves and more) [2]. As such, $K_d(\lambda)$ constrains bio-physical processes such as heating, carbon fluxes, photochemistry and is used as an input in many physical or assimilative biogeochemical models [3] as well as primary production models [4].

Because K_d varies as a function of the Inherent Optical Properties (IOPs) of a water body (mostly absorption (a) and back-scattering (b_b), [5]), many algorithms were developed to retrieve K_d from R_{rs}, either through explicit empirical fits to in-situ data (Standard level-2/level-3 product from NASA/ESA [6, 7]), development of implicit neural-network (NN) based algorithms [8], or using semi-analytical algorithms that first retrieve IOPs and then use them to compute K_d[9, 10]. These algorithms were all tuned to data from either Case-1 and/or Case-2 waters and share a common characteristic: they were constrained and validated with a small number of in-situ data points that are not representative of the global ocean, or with radiative-transfer model runs using a range of input data assumed to represent the global ocean, but whose distribution does not match the spatial distribution of optical properties in the ocean. In a previous study[1], building on previous work[11], we compiled a novel global database of radiometry data at three different wavelengths and for PAR obtained with sensors onboard BGC-Argo profiling floats and matched them to coincident observations from six different satellite sensors (MODIS-Aqua, MODIS-Terra, VIIRS-SNPP, VIIRS-JPSS, OLCI-S3A, OLCI-S3B). Results showed a strong bias in the clearest ocean waters for all three evaluated algorithms (empirical, NN, and semi-empirical) with R_{rs}-derived $K_d(\lambda)$ and $K_d(PAR)$ consistently over-estimated, resulting in an underestimation of the depth to which light penetrates. This persistent bias was attributed to the fact that the in-situ data-sets used to validate the algorithms lacked sufficient observations representing the clearest waters of the global ocean where extremely low K_d values are found.

Since the clearest waters of the world represent a significant portion of the surface area of the global ocean, the goal of this current study is to recompute coefficients of an empirical $K_d(490)$ algorithms and a $K_d(\lambda)$ algorithm using the more globally representative BGC-Argo-float database ranging from very clear oligotrophic waters to Case-2 coastal waters. As these data do not represent all ocean regions equally, we take into account the number of data points collected and their distribution within and across different biogeochemical regions in the recomputation of the coefficients. We then quantify the impact of the revised parametrization of the attenuation coefficient (K_d) from one algorithm on the estimation of Net Primary Productivity (NPP) using three different net primary production algorithms. We find all NPP models to exhibit a significant difference at the global scale when using the new parametrization of the K_d algorithm. Since NPP represents an essential mechanism for sequestering carbon dioxide from the atmosphere into the ocean, earth-system carbon budgets will likely need to be re-adjusted for the detected bias. We have elected to stay away from $K_d(PAR)$ algorithms ([7, 12]) as those depend on the depth where we want the product at, and as one can get an accurate estimate of those from $K_d(\lambda)$ as recently validated with data from profiling float (e.g. [11, 13]).

2 Methods

2.1 Float match-up data-set

We use the same match-up data-set compiled in our previous study [1] available on the Zenodo repository[1]. It contains match-ups of K_d between six different contemporary ocean color satellite sensors and BGC-Argo floats measuring radiometry. Match-up criteria are based on previously published protocols [14].

2.1.1 $K_d(\lambda)$

The details of the method behind the match-up between BGC-Argo float radiometry and satellite R_{rs} are available in [1]. In brief, float-retrieved K_d (herein $K_d^{float}(\lambda)$ is calculated from downwelling irradiance ($E_d(\lambda)$) using an iterative least-squares regression of $E_d(\lambda)$ with depth. This method is preferred to the standard method of extrapolating E_d to the surface to obtain $E_d(\lambda, 0^-)$ and linearly regressing $E_d(\lambda)$ with depth as it avoids introducing bias through the extrapolation. Different techniques for K_d retrieval were evaluated and showed no significant difference in the fidelity of the retrieval [1]. Before retrieving $K_d^{float}(\lambda)$, all $E_d(\lambda)$ profiles were quality controlled following a published protocol [15] which removed effects of passing clouds, wave focusing, and other bias-inducing effects.

2.2 Regional biome-based weighting and statistical metrics

Float coverage and satellite match-ups in the global ocean are unevenly distributed with a substantial proportion of the floats ($\approx 70\%$) in the Western Mediterranean, Eastern Mediterranean and the Southern Ocean (Table 1). Given that the goal of this study is to recompute the algorithms for the global ocean, it is important not to create an additional source of bias by over-fitting the coefficients towards specific regions.

In order to perform this biome-weighting, two parameters need to be taken into account 1) the surface area of each biome ($Area_i$) - available from [16] for biomes 1:17 and computed for the Mediterranean biomes (Table 1) and 2) the number of match-ups in each biome ($N(Area_i)$) - from the float match-up database. An individual weight (W_i) for each specific match-up can then be computed following:

$$W_i = \frac{Area_i}{N(Area_i)} \tag{1}$$

[1] https://www.zenodo.org/record/7015427#.Y5cv3OzMJ-U

Weights for each region are listed in Table 1. Biomes 2 (North Pacific Subtropical Seasonally Stratified) and 17 (Southern Ocean Ice) have less than 15 match-ups (3 and 2 respectively) across all sensors and are therefore not considered in the rest of this study as their very high individual weight would bias the computation of the new coefficients and because they likely have high uncertainties relative to the central tendency in their own region. They are therefore assigned a N/A weight (Table 1).

In order to ensure that the updated algorithms are representative of the global ocean, we used a Monte-Carlo type sub-setting according to the following method: For each sensor, the total number of match-ups in each biome was computed. Within each biome, a certain number of match-ups were extracted in order to obtain a subset that was representative of the percentage of the ocean covered by each biome. The number of match-ups selected in each biome was based on the largest possible amount of match-ups in the biome that had the largest discrepancy between the proportional surface area and the number of actual match-ups. For example, in the case of MODIS-Terra and $K_d(490)$, Biome 4 had the largest discrepancy with only 17 match-ups and a coverage of 12.29% of the ocean. Therefore we selected all 17 match-ups and sub-sampled the other biomes in accordance with the proportional surface area listed in Table 1, for a total number of 135 match-ups. This was repeated 100 times (each time picking random match-ups from each biome), in order to compile a "proportional dataset" for each sensor that was proportionally representative of the global dataset. Statistical metrics were computed over the total proportional dataset for each sensor.

Statistical metrics on the whole (unweighted) dataset, not taking into account uneven coverage, are found in the Supplementary material for comparison purposes (Table S1).

Table 1: Area and proportion of the global ocean represented by each Oceanic biome based on [16] and with the two Mediterramean biomes added. The total number of match-ups for the full data-set is reported (with all sensors combined), and the individual weight for each float-Satellite match-up is reported based on the number of match-ups in one specific biome, as well as its relative area as described in equation 1. Biomes 1,2,3,5 and 17 have less than 15 match-ups and were therefore considered "empty" for the rest of this study, so as not to skew the fitting coefficient of the new parametrization for attenuation algorithms.

Biome Name	**Biome Number**	**Area (10^6 km^2)**	**Proportion of total area (%)**	**Number of match-ups**	**Individual weight of match-ups**
North Pacific Ice	1	4.59	1.37	0	N/A
North Pacific Subpolar Seasonally Stratified	2	12.84	3.85	3	N/A
North Pacific Subtropical Seasonally Stratified	3	6.83	2.04	0	N/A
North Pacific Subtropical Permanently Stratified	4	41.05	12.29	170	0.072
West pacific Equatorial	5	11.69	3.50	0	N/A
East Pacific Equatorial	6	14.89	4.46	102	0.044
South Pacific Subtropical Permanently Stratified	7	52.71	15.79	434	0.036
North Atlantic Ice	8	5.48	1.64	225	0.007
North Atlantic Subpolar Seasonally Stratified	9	10.06	3.01	690	0.004
North Atlantic Subtropical Seasonally Stratified	10	5.97	1.79	22	0.081
North Atlantic Subtropical Permanently Stratified	11	17.46	5.23	436	0.012
Atlantic Equatorial	12	7.41	2.22	23	0.097
South Atlantic Subtropical Permanently Stratified	13	18.06	5.41	704	0.008
Indian Ocean Subtropical Permanently Stratified	14	35.94	10.76	16	0.673
Southern Ocean Subtropical Seasonally Stratified	15	29.69	8.89	380	0.023
Southern Ocean Subpolar Seasonally Stratified	16	39.63	11.87	305	0.039
Southern Ocean Ice	17	18.68	5.59	2	N/A
Western Mediterranean	18	0.73	0.22	2493	8.8×10^{-5}
Eastern Mediterranean	19	1.86	0.56	2969	1.9×10^{-4}

2.3 Updated algorithms for R_{rs}-retrieval of $K_d(\lambda)$

2.3.1 Empirical algorithms used for the operational products.

Two different algorithms computing $K_d(490)$ evaluated in [1] and their associated coefficients are here re-parameterized. The first is the operational level-2 and level-3 product for $K_d(490)$ of both NASA and ESA. Although two distinct products, both are based on the same empirically-derived link between in-situ $K_d(490)$ measurements and blue-to-green R_{rs} band ratio [6], originally developed for CZCS with "blue" defined as the wavelength closest to $490nm$ and "green" the sensor's wavelength between $547nm$ and $565nm$. NASA's version[2] is computed as follows, with the A_i coefficients tuned to each specific sensor, and $K_w(490) = 0.0166\, m^{-1}$ being the value used for the diffuse attenuation

[2] https://oceancolor.gsfc.nasa.gov/atbd/kd_490/

at $490nm$ due to seawater.

$$K_d(490)^{NASA} = K_w(490) + 10^{A_0 + \Sigma_{i=1}^{4} A_i \left(\log_{10}\left(\frac{R_{rs}(\lambda_{blue})}{R_{rs}(\lambda_{green})}\right)\right)^i} \quad (2)$$

ESA's version also uses $K_w(490)$, five A_i coefficients, and a blue-to-green reflectance ratio based on [7].

$$K_d(490)^{ESA} = K_w(490) + 10^{\Sigma_{i=0}^{4} A_i \left(\left(\log_{10}\left(\frac{R_{rs}(490)}{R_{rs}(560)}\right)\right)\right)^i} \quad (3)$$

For the sake of comparison, NASA's and ESA's empirical products (applied to their respective sensors) will be grouped together in the statistical metrics and referred to as $K_d(490)^{NASA/ESA}$.

2.3.2 Semi-Analytical algorithm based on IOP retrieval.

$K_d(\lambda)$ retrieval from the semi-analytical algorithm (herein $K_d(\lambda)^{QAA}$) was first published in 2005 [9] and refined in 2013 [10]. It is based on the relationship between $K_d(\lambda)$, IOPs, and the solar zenith angle (θ). It was constrained using Hydrolight simulations using the synthetic IOCCG data-set [17]. The IOPs for absorption ($a(\lambda)$) and backscattering ($b_b(\lambda)$) at any wavelength are retrieved from $R_{rs}(\lambda)$ using the Quasi-analytical algorithm (QAA) [18] version 6 [3] with $\eta_w(\lambda) = b_{b_w}(\lambda)/b_b(\lambda)$:

$$K_d^{QAA}(\lambda) = (1 + 0.005\theta) \times a(\lambda) + (1 - A_1 \times \eta_w(\lambda)) \times A_2 \times \left(1 - A_3 \times e^{-A_4 \times a(\lambda)}\right) \times b_b(\lambda). \quad (4)$$

Pure water absorption values are retrieved from [19] and pure water backscattering is corrected for the effect of salinity following [20]. Here we recompute the value of the A_i coefficients based on the match-ups at 490nm and keep the coefficient relating to the sun angle (0.005 in equation 4). For other wavelengths the coefficients should be the same (as in Lee's paper [10]).

2.4 Independent validation data-sets

Recomputed $K_d(\lambda)s$ ($K_d(\lambda)^{R_{rs}}_{NewCoeffs}$) were independently evaluated with existing in-situ and synthetic data-sets commonly used in global K_d algorithms development. The NOMAD (NASA bio-Optical Marine Algorithm Data set) data-set [21] is an in-situ data-set spanning oligotrophic to eutrophic waters and has been used to develop the operational empirical R_{rs}-retrieved $Kd(490)$ level-2/level-3 product from NASA[4] and contains about 800 simultaneous $E_d(\lambda)$ and $R_{rs}(\lambda)$ measurements. The COASTLOOC data-set consists of oligotrophic to eutrophic measurements in European waters and contains 195 pairs of reflectance below the surface ($R(0^-, \lambda)$) and $K_d(\lambda)$. $R(0^-, \lambda)$ was converted to R_{rs} with $R_{rs} = 0.133 \times R(0^-, \lambda)$ following [22]. The International Ocean Color Coordinating Group (IOCCG)'s synthetic data-set, originally designed to develop and validate inversion algorithms [2, 17] was also used, where data points simulate natural variability over a wide range of Case-1 and Case-2 waters. One thousand paired $R_{rs}(\lambda)$, $K_d(\lambda)$ and associated IOPs such as $a(\lambda)$ and $b_b(\lambda)$ are available from this dataset. All three of these data-sets are independent and have varying ranges different from the newly-compiled float database [1]. Therefore, they should be

[3] (https://www.ioccg.org/groups/Software_OCA/QAA_v6_2014209.pdf),
[4] https://seabass.gsfc.nasa.gov/wiki/NOMAD

able to assess the robustness of the new coefficients across a different dynamic range than they were derived with (higher percentage of high values, strong bias towards specific biomes).

Since coefficients for the $K_d^{QAA}(490)$ algorithm are recomputed using $K_d(490)^{float}$, applying the same coefficients to assess the accuracy of retrieval at another wavelength (such as $412nm$ to retrieve $K_d(412)$) provides an additional independent validation for the performance of the new formulation.

2.5 Cost functions used for each algorithm

New coefficients were computed for the two $K_d(\lambda)^{R_{rs}}$ and the $K_d(PAR)^{R_{rs}}$ algorithms by minimizing the following cost function:

$$\overline{\chi} = \sum_{i=0}^{N(match-ups)} W_i * \frac{\left|K_d(\lambda, i)^{R_{rs}}_{NewCoeffs} - K_d(\lambda, i)^{float}\right|}{Uncertainty_i} \tag{5}$$

where W_i is the individual biome-weight of each match-up (see equation 1), $Uncertainty_i$ for a given match-up defined as the maximum value between a minimum constant uncertainty (0.005) due to sensor specificity and a percentage (10%) of $K_d(\lambda)^{R_{rs}}$: $Uncertainty_i = max(0.005m^{-1}, 0.1 * K_d(\lambda)^{R_{rs}})$ and $K_d(\lambda)^{R_{rs}}_{NewCoeffs}$ is derived from equations 2, 3, and 4, depending on the algorithm evaluated. The set of coefficients $A_i, i = 1:5$ resulting in the smallest cost function $\overline{\chi}$ is considered as resulting in the best retrieval for our data-set and are termed the "new coefficients" (available in Table S2). The uncertainty formulations is designed to have an absolute error at low values and proportional error at larger values as will be expected as a result of uncertainties that are both instrumental and environmental.

Unlike $K_d(490)^{NASA/ESA}$, $K_d(490)^{QAA}$ was initially developed [9] with one single set of coefficients for all satellite sensors. To ensure that using a "sensor-specific" set of coefficients (found in Table S2) for each satellite wasn't resulting in a bias in $K_d(490)$ retrieval between different sensors, we tested the retrieval of $K_d(490)^{QAA}$ for each sensor using level-3 gridded R_{rs} from each sensor for the month of July 2020. The same method of retrieving the IOPs from R_{rs} using QAA and subsequently computing K_d was used for each sensor. The idea was to assess how each sensor-pair would retrieve K_d with their own input data (R_{rs}), and if using the sensor-specific coefficients resulted in a different distribution between sensors-pairs than when using the same coefficients for all sensors (in this case the specific ones derived for MODIS-Aqua). Statistical metrics were computed for both cases "same coefficients" and "sensor-specific coefficients" and are found in the Supplementary (Table S3).

2.6 Net Primary Production (NPP) models

To evaluate the impact of the revised $K_d(490)^{QAA}$ algorithm, we implemented it into two commonly used, global NPP models. We chose to evaluate solely $K_d(490)^{QAA}$, as the new parametrization yields similar performance to $K_d(490)^{NASA/ESA}$ and is more adapted to a global ocean with both Case-1 and Case-2 waters. The first model is the Vertically Generalized Production Model (VGPM). The VGPM is a chlorophyll-based model that relies on chlorophyll a (Chl a) concentration, day length, the maximum possible rate of primary production at a given location (derived from Sea Surface Temperature (SST)), and a light-dependent function [23].

The Carbon-based Productivity Model (CbPM) computes phytoplankton biomass from particulate back-scattering (b_{bp}) and estimates growth rate (μ) from the observed chlorophyll to carbon ratio [24] compared to the median mixed layer irradiance. The updated version (CbPMv2) is used here [4], which attenuates light spectrally throughout the water column.

There are notable differences regarding the input of $K_d(490)^{QAA}$ between these models and how it is used; in both, monthly gridded $K_d(490)^{QAA}_{NewCoeffs}$ / $K_d(490)^{QAA}_{Original}$ computed using QAA-retrieved a and b_b from R_{rs} are used as inputs. In VGPM, $K_d(490)$ is converted into $K_d(PAR)$ using Morel's algorithm [7] for a layer of thickness $1/K_d(490)\,m$. In CbPMv2, $K_d(490)$ is used to compute a spectral $K_d(\lambda)$.

Monthly mapped level-3 ocean color climatology from MODIS-Aqua were downloaded from the NASA Ocean Biology Distributed Active Archive Center (OB.DAAC)[5] for the whole mission. Monthly mixed-layer depths for 2021 required as input in the CbPM model were calculated from the data-assimilative HYCOM model output (using a density threshold of 0.03 $kg.m^{-3}$ criteria) and were downloaded from the Ocean Productivity webpage[6]. Monthly nitrate climatological profiles were downloaded from the World Ocean Atlas select [25] (WOAselect) and nitracline depths were defined as the depth at which nitrate concentration $(NO_3) > 0.3\mu M$ per [4]. Climatology of $K_d(490)^{QAA}_{NewCoeffs}$ and $K_d(490)^{QAA}_{Original}$ were computed using L3 R_{rs} data from NASA's OB.DAAC to use as inputs in the NPP models. The new coefficients chosen to compute $K_d(490)^{QAA}_{NewCoeffs}$ were the ones recomputed for MODIS-Aqua.

When performing the annual assessment, monthly data (for the whole 20-year climatology) were averaged for each pixel. We compare the models by performing a single modification; either we use $K_d(490)^{R_{rs}}_{NewCoeffs}$ or $K_d(490)^{R_{rs}}_{Original}$, all other inputs were kept exactly the same. When computing the average percent difference over a given month, the sum of the difference was divided by the number of pixels with existing NPP data either in the whole ocean (for the global comparison) or in regions with either low ($K_d(490) < 0.026\,m^{-1}$) or high ($K_d(490) > 0.1\,m^{-1}$) $K_d(490)$ (for the regional analysis). All results reported here were weighted to account for the latitudinal changes in the pixel area.

[5] https://oceancolor.gsfc.nasa.gov/l3/order/

[6] http://sites.science.oregonstate.edu/ocean.productivity/index.php

3 Results

3.1 $K_d(490)$ retrieval

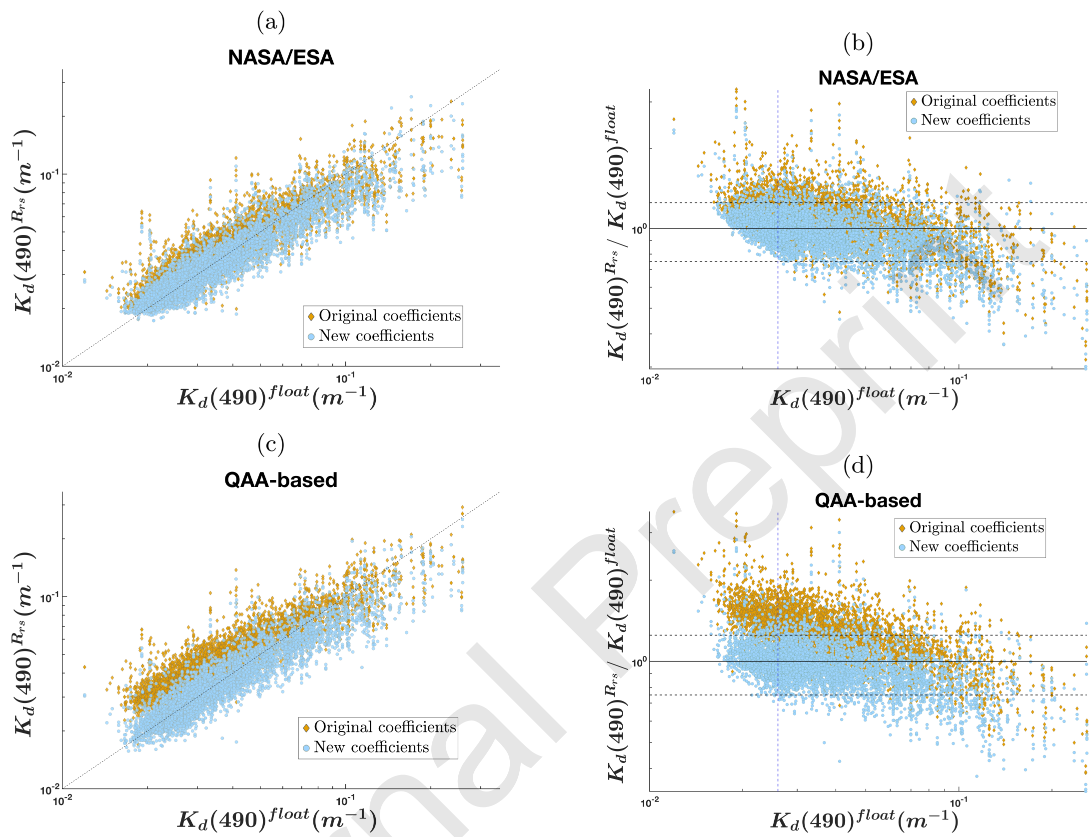

Figure 1: Comparison of $K_d^{R_{rs}}$ retrieval for the full match-up data-set (with all sensors grouped together) from two different algorithms with the newly computed vs. the original coefficients. (a) $K_d(490)^{R_{rs}}_{NASA/ESA}$ compared to $K_d(490)^{float}$. (b) Error ratio of $K_d(490)^{R_{rs}}_{NASA/ESA}$ to $K_d(490)^{float}$.(c) $K_d(490)^{R_{rs}}_{QAA}$ compared to $K_d(490)^{float}$. (d) Error ratio of $K_d(490)^{R_{rs}}_{QAA}$ to $K_d(490)^{float}$. New coefficients are listed in Table S2. The blue vertical line in (b) and (d) is 0.026, the minimum value of $K_d(490)$ in the NOMAD dataset.

Overall, for most satellite sensors the new coefficients resulted in an improvement for both algorithms ($K_d(490)^{NASA/ESA}$ and $K_d(490)^{QAA}$) with a bias closer to one and a lower ADP (Table 2), at the exception of OLCI-S3A for $K_d(490)^{NASA/ESA}$.

$K_d(490)^{QAA}_{NewCoeffs}$ performs similarly to $K_d(490)^{NASA/ESA}_{NewCoeffs}$ for all measured statistical metrics and has a slope closer to one. The bias for the low values of $K_d(490) < 0.026\, m^{-1}$ is no longer present although there appears to be a larger error ratio for some of the higher $K_d(490)$ values than with $K_d(490)^{R_{rs}}_{Original}$ (Figure 1). The number of match-ups with an error ratio (normalized difference between $K_d(490)^{R_{rs}}$ and $K_d(490)^{float}$) larger than ±25% when comparing the new vs. original coefficients decreased from 25% to 17% for $K_d(490)^{NASA/ESA}$ and from 60% to 17% for

Table 2: Statistics for $K_d(490)^{Rrs}$ vs $K_d(490)^{float}$ for each of the six studied satellite sensors. For each sensor, a sub-sample was extracted at random to create an ensemble that has a proportion of data points from each biome consistent with the area covered by each biome. 100 ensembles (with random data points from each biome extracted every time) were added together to recreate a dataset representative (in proportion) of the ocean. Statistical metrics were computed on this proportional dataset. Bias is the median of the ratio between $K_d^{R_{rs}}$ and K_d^{float}, Average Percent Difference (ADP) is as defined in [9], Root Mean Square Difference (RMSE) as defined in [8] and the slope between the log of the values is retrieved after performing a robust (bi-square weighting function) linear fit using the Matlab integrated function $fitlm$.

	NASA / ESA $K_d(490)$											
	MODIS-Terra		**MODIS-Aqua**		**VIRRS-SNPP**		**VIIRS-JPSS**		**OLCI-S3A**		**OLCI-S3B**	
Coefficients	Old	New	Old	New	Old	New	Old	New	Old	New	Old	New
Bias	1.17	1.00	1.18	1.00	1.08	0.98	1.07	0.99	1.02	0.93	1.17	1.00
ADP (%)	21.76	14.39	22.79	14.53	15.84	14.74	15.81	14.41	16.71	18.79	16.88	9.72
RMSE	0.01	0.01	0.01	0.01	0.01	0.01	0.01	0.01	0.01	0.02	0.01	0.01
r	0.87	0.87	0.88	0.88	0.87	0.87	0.91	0.91	0.74	0.74	0.95	0.97
Slope	0.95	1.00	0.95	0.99	0.98	1.01	0.98	1.00	0.98	1.01	0.96	1.00
	QAA-based $K_d(490)$											
	MODIS-Terra		**MODIS-Aqua**		**VIRRS-SNPP**		**VIIRS-JPSS**		**OLCI-S3A**		**OLCI-S3B**	
Coefficients	Old	New	Old	New	Old	New	Old	New	Old	New	Old	New
Bias	1.26	1.01	1.38	0.98	1.37	0.98	1.34	0.96	1.33	0.96	1.43	1.00
ADP (%)	29.67	14.77	38.55	16.03	37.82	14.06	34.88	14.27	33.47	14.17	38.90	12.59
RMSE	0.01	0.01	0.02	0.01	0.02	0.01	0.01	0.01	0.02	0.02	0.01	0.01
r	0.86	0.86	0.86	0.85	0.88	0.87	0.91	0.91	0.78	0.77	0.94	0.94
Slope	0.93	0.99	0.91	1.00	0.90	1.00	0.91	1.01	0.92	1.00	0.90	1.00

$K_d(490)^{QAA}$.

3.2 Independent validation

Since the float data-set was used in the derivation of the new coefficients there isn't complete independence between the two. We note, however, that the number of degrees of freedom in the data-set is much larger than the number of fitting coefficients computed, and hence they may be considered as, de-facto, independent.

In any case, the new coefficients were also validated in two additional ways. First, we used the same float data-set but assessed the performance of the QAA-based algorithm at a different wavelength, 412 nm. Since the coefficients were re-computed and fitted only using the 490 nm, $K_d(412)^{QAA}$ retrieval using those same coefficients is independent (as the $K_d(412)^{R_{rs}}$ $/K_d(412)^{float}$ match-ups were not used in the derivation of the new coefficient). There is a very significant improvement in retrieval for $K_d(412)$, with a smaller bias, a smaller ADP by 29%, a smaller RMSE, and a slope closer to 1 (Figure 2), with the small-value bias significantly better as only 28 % of the new coefficient values have an error ratio of $\pm25\%$ now (compared to $\approx 70\%$ for the original coefficients).

The second way in which the new coefficients were independently assessed was by application to other data-sets of R_{rs}-$K_d(490)$ match-ups used to derive and assess K_d algorithms. The NOMAD, COASTLOOC, and synthetic IOCCG data span conditions from Case-1 to Case-2 waters and have a different statistical distribution than the float matchup database [1]. Performance in $K_d(490)$-

retrieval of those three databases decreases to some extent with the new coefficients: they result in a higher ADP and RMSE (Figure 2) and a larger absolute bias. The new coefficients tend to underestimate $K_d(490)$. There are no significant differences in retrieval performance with the new coefficients when considering the full in-situ datasets or when selecting only data points corresponding to a Case-2 water type from the IOCCG, NOMAD and COASTLOOC datasets : in both cases the new coefficients perform less well. Note, however, that we have not weighted the performance metrics by the area of the oceans they are representing.

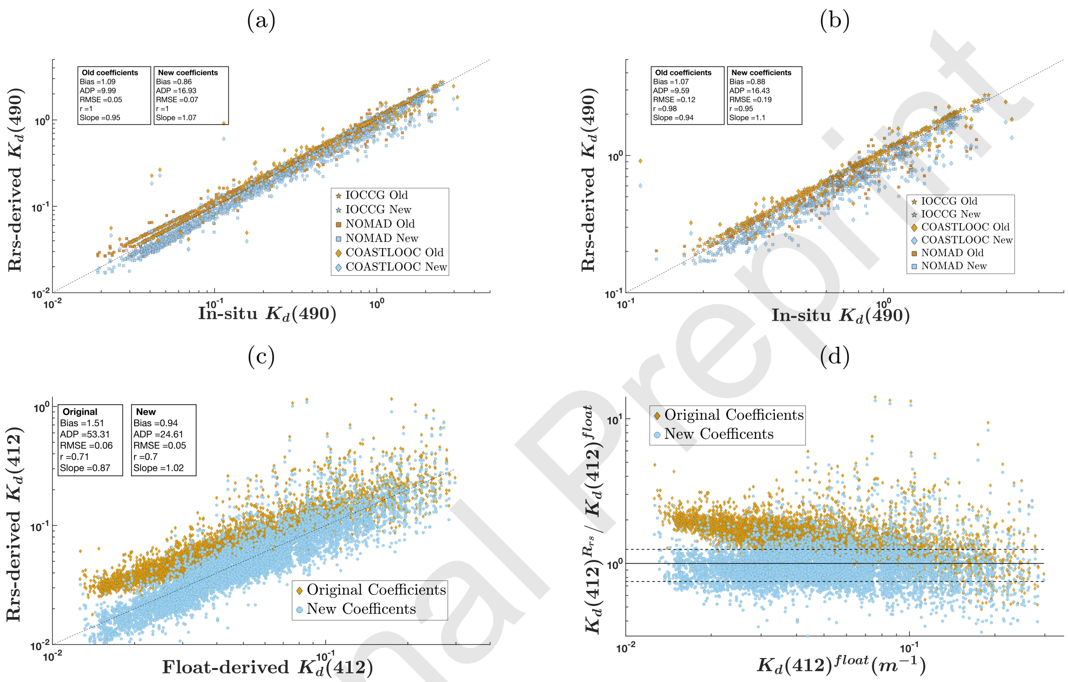

Figure 2: Comparisons between $K_d(\lambda)^{QAA}$ and $K_d(\lambda)^{inSitu}$ for independent databases not used in the computation of the new coefficients. (a) $K_d(490)^{QAA}$ versus $K_d(490)^{InSitu}$ with the original (Old) and the New coefficients. Shown here are NOMAD, COASTLOOC and the synthetic IOCCG database comparisons for the full data-sets. (b) $K_d(490)^{QAA}$ versus $K_d(490)^{InSitu}$ with the original (Old) and the New coefficients on Case-2 waters from the COASTLOOC and the synthetic IOCCG databases. (c) $Kd(412)^{QAA}$ versus $Kd(412)^{float}$ for the Original (orange) and the New (blue) coefficients. (d) Error ratio of $Kd(412)^{QAA}/\ Kd(412)^{float}$ for the Original (orange) and the New (blue) QAA coefficients.

3.3 Impact of new coefficients on Global Primary production quantification

3.3.1 Annual comparison

Annual percentage differences between using $K_d(490)^{QAA}_{Original}$ or $K_d(490)^{QAA}_{NewCoeffs}$ (the difference between the two $K_d(490)^{QAA}$ will be referenced to as $K_d(490)^{QAA}_{Diff}$) as inputs in each of the two primary production models were computed; for VGPM (hereafter called ΔNPP_{VGPM}), the overall difference for the annual time series NPP shows a seasonal signal in areas with low $K_d(490)$ (Figure 3), and to a lesser extent in areas with high $K_d(490)$. For the low $K_d(490)$ areas (defined as $K_d(490) < 0.026\,m^{-1}$), we note a higher-than-average difference between original and new coefficients, with a relative annual mean difference value of $\approx$ 79.2 %, and an absolute annual production difference of 7.88 $Pg\,C.yr^{-1}$. The percent difference is larger in the summer months for each hemisphere, with a maximum increase in late Spring and early Fall for the North Hemisphere. For the high $K_d(490)$ values (defined as $K_d(490) > 0.1 m^{-1}$), the annual difference is significantly lower, with an average of $\approx$ - 10%. The spatial pattern of difference in NPP retrieved from the VGPM model is correlated with the pattern of $K_d(490)^{QAA}_{Diff}$. The extent of ΔNPP_{VGPM} is similar to $K_d(490)^{QAA}_{Diff}$, with a smaller relative difference in the productive areas characterized by a large $K_d(490)$ and a large NPP_{VGPM} (such as the high latitudes of the northern hemisphere) and the highest difference in the areas with low $K_d(490)$ such as the subtropical gyres (Figure 3). When summing all data points within the climatology and weighting by each 1° pixel area, ΔNPP_{VGPM} is 35.53%, that is the use of $K_d(490)^{QAA}_{NewCoeffs}$ results a $\approx$ 35% increase in the estimate of global primary production (increasing from 38.32 $Pg\,C.yr^{-1}$ to 53.86 $Pg\,C.yr^{-1}$).

The effect of changing $K_d(490)$ in CbPMv2 is different than of VGPM. ΔNPP_{CbPM} has an average yearly difference in primary production of 38.66 %; production increased from 55.66 $Pg\,C.yr^{-1}$ (using $K_d(490)^{QAA}_{Original}$) to 77.18 $Pg\,C.yr^{-1}$ (using $K_d(490)^{QAA}_{NewCoeffs}$). The maximum percentage difference is in the Southern Ocean and the North Atlantic (Figure 3). Regions of low $K_d(490)$ show a difference of 38.71%, an increase of 7.19$Pg\,C.yr^{-1}$, consistent with the results from VGPM. In High $K_d(490)$ areas ($> 0.1\,m^{-1}$), ΔNPP_{CbPM} is also smaller on average (19.32%).

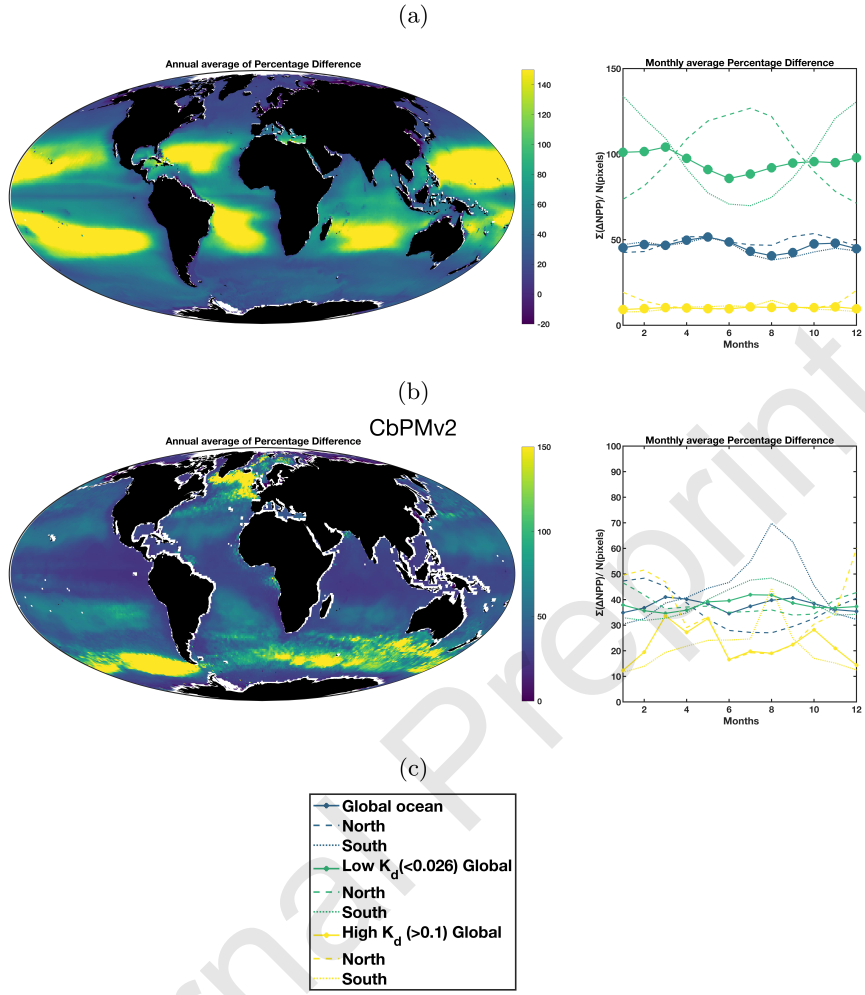

Figure 3: Difference in annual average NPP when using the original vs. the new coefficients as inputs in $K_d(490)^{QAA}$ using different Primary Production models. The left side is a map of the annual average percentage difference (%) and the right side is time series across months for regions with low $K_d(490)^{QAA}(< 0.026)$, high $K_d(490)^{QAA}(> 0.1)$ and for the overall region. Separation within each region is made for the North and South hemisphere to better represent seasonality. (a) Vertically Generalized Production Model (VGPM). (b) Carbon-based Productivity Model version 2 (CbPMv2). (c) Legend for the yearly climatology.

4 Discussion

In this work, we set as our goal to derive new coefficients for existing algorithms for $K_d(\lambda)$ so that they would be less biased *globally*. The use of weights in the fitting was designed so that the size of each biome and the number of match-ups within said biomes are taken into account. Additionally, we assumed a specific uncertainty for the fit (proportional to K_d except at low values) and minimized a cost function based on absolute difference. This, of course, means that the fit is *different* from that which would be derived by weighing all match-ups equally, assuming the same uncertainty for all points and minimizing a cost-function based on root-mean-square.

A bias for small values of $K_d(490)$ had already been identified in previous studies, albeit with different cutoff values ($0.03\,m^{-1}$in [8] and $0.026\,m^{-1}$ in [1]) but had not been addressed as it represented a minimal proportion of the in-situ or simulated data-sets evaluated. However, a significant area of the ocean is characterized by clear waters with low $K_d(\lambda)$. Using the new coefficients we find the area where $K_d(490)^{QAA}_{NewCoeffs} < 0.026\,m^{-1}$ during the climatology to represent 33% of the ocean (versus 0% with the original coefficients) and $K_d(490)^{NASA/ESA}_{NewCoeffs} < 0.026\,m^{-1}$ represents 38% of the ocean (versus 24% for the original coefficients). Although primary production and carbon export are lower in these clear-water regions, the large areas they represent means that this bias is likely to have a significant impact on the quantification of physical and biological processes.

4.1 Improvement matching K_d for the BGC-Argo data-set

Using the new K_d coefficients resulted in significant improvement in the statistical metrics of match-ups between floats and satellites at the global scale, but the improvement varied depending on the algorithm and the sensor. $K_d(490)^{NASA/ESA}$ showed the smallest improvement, but it was still significant at the individual sensor level. The Austin and Petzold algorithm upon which $K_d(490)^{NASA/ESA}$ is based was designed to work on clear Case-1 open-ocean waters so it is not surprising that it performs relatively well on the float data-set that is exclusively comprised of open-ocean measurements. The fact that there remains a bias (although of decreased amplitude) for low values when using the newly computed best-fit coefficients (Figure 1) is likely due to two factors: 1) The small values have a relatively low weight in the overall cost function, meaning that the cost function will try to minimize the bias for larger K_d values in priority (since they represent larger under-sampled ocean regions) and 2) the coefficients in the $NASA/ESA$ algorithm are related to the blue/green band ratio of R_{rs}. The ratio might not be able to encompass the variability in K_d that is due to other parameters than the blue/green ratio (which is directly linked to the Chlorophyll a content of a water body [26]) such as the presence of high concentrations of Colored Dissolved Organic Matter (CDOM), Total Suspended Matter (TSM), and the effect of solar angle among others. Therefore, there would be limitations in the algorithm design itself, rather than in the coefficient recalculation per-se. Additionally, the blue/green spectral ratio follows an asymptotic shape, meaning that once it reaches a certain value of $K_d(490)$, the ratio will no longer be influenced by changes in $K_d(490)$ [9]. The limitations of the NASA/ESA empirical algorithms are well documented and it is widely accepted to be only suitable for Case-1 relatively clear open ocean waters [8, 9, 27].

On the other hand, the semi-analytical algorithm generating $K_d(\lambda)^{QAA}$ was developed to work on a wide variety of waters and at all visible wavelengths, which means that the original range for which it was designed is much larger than for $K_d(490)^{NASA/ESA}$. However, no data used in either the computation of its original coefficients or the validation had values of $K_d(490)$ below $0.026m^{-1}$ [1, 9, 10] which likely caused the bias for small K_d values when the original coefficients were used. This bias was mostly resolved here, resulting in the number of match-ups with an error ratio greater than 25% going from 60% to 17 %, which shows that using IOPs and solar angle might be a more robust way to retrieve $K_d(\lambda)$ than the link between $K_d(490)$ and a reflectance ratio associated with chlorophyll change when aiming to accurately retrieve the full range of variability found in nature. Although the small value bias appears to be resolved by the use of the new coefficients, the larger values in our data-set ($K_d(490) > 0.1\, m^{-1}$) are more under-estimated than previously. Again, this appears to be due to the fact that they do have a lower weight in the final computation.

The limited geographical area covered by the data in NOMAD (Gulf of Mexico, Eastern Coastal US, Pacific gyre and Mediterranean Sea) and COASTLOOC (Mediterranean Sea, Eastern and Coastal North Artlantic) means that they can almost be considered as a regional dataset. Given that we tried to recompute coefficients that work for the whole ocean, it is not surprising that a "regional" algorithm performs better than a global one in the specific region it was developed. The fact that there is little difference in the retrieval for the full datasets versus for the Case-2 water types using the new coefficients suggests that the modified algorithm is able to accurately retrieve Case-2 waters even though it wasn't derived with such data. However, we see a large variability in the new coefficients that were computed between sensors (Table S2). This leads to the conclusion that there may be too many coefficients tuned in this algorithm, resulting in several "solutions" when trying to determine the best coefficients that allow to compute $K_d(\lambda)$ from $a(\lambda)$ and $b_b(\lambda)$. Future work could explore if adjusting the number of coefficients and/or its explicit formalism could improve this algorithm .

Using sensor-specific coefficients versus one set of coefficients as inputs in $K_d(490)^{QAA}$ did result in slight differences between sensor-pairs (Table S3). Metrics indicate that using sensor-specific coefficients might result in slightly different retrieval of $K_d(490)$, which means that when using different satellite sensors to retrieve $K_d(\lambda)$, using the globally-derived coefficients (found in Table S2) might ensure a consistent retrieval between sensors.

4.2 Quantification of the bias in NPP

To assess the impact of the new algorithm, two different satellite-based primary production models were evaluated. The objective here was not to compare the performance of those models and assess which one was the closest to reality but to quantify how the change in $K_d(490)$ computation propagates to a change in primary production obtained from each individual model. VGPM's NPP, by design, is correlated with $K_d(490)$ [23] (Figure S4). Since the largest difference between $K_d(490)^{QAA}_{NewCoeffs}$ and $K_d(490)^{QAA}_{Original}$ occurs for small $K_d(490)$ values (Figure 1), the oligotrophic gyres show the highest ΔNPP_{VGPM} due to the underestimation of the euphotic depth. High $K_d(490)$ areas even show a small decrease in NPP ($-0.62\, Pg\, C.yr^{-1}$), consistent with the pattern in $K_d(490)^{Diff}$.

Another notable feature in areas characterized by low $K_d(490)$, visible in the outputs of both VGPM and CbPMv2 , is the presence of a seasonal cycle in ΔNPP. Between summer (higher ΔNPP) and winter (lower ΔNPP), there are differences of $\approx$ 50% for VGPM and $\approx$ 20% for CbPMv2 (Figure 3).

The seasonal cycle in difference can also be attributed to the change in $K_d(490)$ in those oligotrophic waters, where $K_d(490)$ is strongly correlated with Chl a. In winter there is higher Chl a (associated with a higher biomass of phytoplankton and/or photo-acclimation), resulting in a larger $K_d(490)$. On the other hand, summer is characterized by stratified, nutrient-limited waters, supporting a smaller amount of biomass of high-light adapted cells, effectively leading to a lower $K_d(490)$ [28]. Since smaller $K_d(490)^{QAA}$ values have a larger bias than higher values, there are larger ΔNPP_{VGPM} and ΔNPP_{CbPM} in the summer than in winter. This effect is not as pronounced for the high $K_d(490)$ areas (defined here as $K_d(490) > 0.1 m^{-1}$) for VGPM ($\approx$ - 10 %) since the bias was smaller originally, and the reparametrization shows a slight overestimation of high $K_d(490)$ values, which explains why there is a small decrease in yearly NPP in those regions.

CbPMv2 shows a very different spatial pattern than VGPM models, with ΔNPP_{CbPM} maximal in regions associated with deep winter mixing. The design of the CbPMv2 model explains why it behaves in a different manner: since NPP is integrated with depth until the bottom of the mixed layer, the larger the layer, the larger the change in the amount of light (here our $\Delta K_d(490)$) will have an effect (as it will propagate through the layer). It is important to note that those areas with a very large mixed layer resulting in a large percentage change in NPP are in fact not very productive, as they are limited by light availability. Therefore even if the percentage change is very high (Figure 3), the magnitude of the effect of $\Delta K_d(490)$ is small in those areas (high $K_d(490)$ areas show an overall increase of 1.70 to 2.03 $Pg\,C.yr^{-1}$ when changing the coefficients and the maximum median monthly difference for the Southern hemisphere is in August and has an amplitude of 70%), which explains why ΔNPP_{CbPM} (38.71 %) is not much larger than ΔNPP_{VGPM} (35.53 %), despite having areas where annual average percentage differences reaching ¿ 150% in the North Atlantic and in the Southern Ocean (notably due to deep convective mixing in the North Atlantic Ocean).

Subtropical gyres represent 41% of the global ocean surface [29]. Numerous studies have attempted to quantify NPP in the gyres either with in-situ measurements [29] or using models [30, 31] or both [32]. Estimates have historically ranged from 125 - 450 $mg\,C^{-2}\,d^{-1}$ [32]. Our findings show the largest discrepancy between the new and original K_d coefficients for the VGPM model happens in the subtropical gyres (characterized by very clear waters with small K_ds), and that it has a non-negligible impact on the overall global primary production. Our results also indicate that the subtropical gyres are responsible for a higher proportion of the global productivity of the ocean and that their role has been previously underestimated. Updating the K_d coefficients and applying them to the gyres' NPP estimates results in a net annual production change ranging from 7.19 $Pg\,C.yr^{-1}$ (CbPMv2) to 7.88 $Pg\,C.yr^{-1}$ (VGPM). In the context of a changing climate, with the warming of the surface ocean and the associated decrease of vertical mixing, subtropical gyres are expected to increase in area [33] and their NPP is expected to decrease [34]. It is thus important to monitor how NPP changes in these areas with un-biased algorithms.

5 Summary

This study derived new coefficients for the computation of the spectral and planar diffuse attenuation of exiting algorithms, making them more consistent globally. Using these new coefficients within commonly-used diffuse attenuation models ($NASA/ESA$, QAA) improves their performance in optical water types ranging from Case-1 to Case-2. Previously computed attenuation coefficients were significantly over-estimated, resulting in an under-estimation of the depth to which light penetrates in oligotrophic waters, particularly in the subtropical gyres. The effect of the newly-computed $K_d(490)$ on different NPP algorithms suggests that NPP was underestimated in the gyres by as much as 38% (CbPMv2 model) to 79.20% (CbPMv2 model). This results in a global bias in NPP. As explained in [1], the underlying reason for the bias in attenuation was the lack of training data for algorithms from clear ocean regions and thus efforts should be made to continue to gather data representative of all areas of the oceans. BGC-Argo floats have been proven to be a very valuable tool for validation of global satellite products and here for their improvement and further deployments should be encouraged, as many regions of the globe are still under-sampled (e.g. the equatorial Pacific Ocean, [1]).

6 Supplementary

Table S1: Statistics for $K_d(490)^{Rrs}$ vs $K_d(490)^{float}$ for each of the six studied satellite sensors as well as for the full data-set. Bias is the median of the ratio between $K_d^{R_{rs}}$ and K_d^{float}, Average Percent Difference (ADP) is as defined in [9], Root Mean Square Difference (RMSE) as defined in [8] and the slope and intercept value are retrieved after performing a robust (bisquare weighting function) linear fit using the Matlab integrated function $fitlm$.

	NASA / ESA $K_d(490)$											
	MODIS-Terra		**MODIS-Aqua**		**VIRRS-SNPP**		**VIIRS-JPSS**		**OLCI-S3A**		**OLCI-S3B**	
Coefficients	Old	New	Old	New	Old	New	Old	New	Old	New	Old	New
Bias	1.13	0.97	1.12	0.96	1.06	0.95	1.04	0.97	1.09	1.00	1.19	1.05
ADP (%)	20.53	16.74	19.76	16.52	17.33	16.69	17.10	16.12	18.47	16.46	22.08	16.76
RMSE	0.01	0.02	0.01	0.02	0.01	0.02	0.01	0.01	0.01	0.01	0.01	0.01
r	0.90	0.90	0.89	0.87	0.88	0.88	0.92	0.92	0.83	0.83	0.91	0.91
Slope	0.96	1.00	0.96	1.01	0.98	1.01	0.99	1.01	0.97	1.00	0.95	0.98
	QAA-based $K_d(490)$											
	MODIS-Terra		**MODIS-Aqua**		**VIRRS-SNPP**		**VIIRS-JPSS**		**OLCI-S3A**		**OLCI-S3B**	
Coefficients	Old	New	Old	New	Old	New	Old	New	Old	New	Old	New
Bias	1.27	1.01	1.37	0.99	1.36	0.98	1.34	0.96	1.33	1.00	1.39	1.00
ADP (%)	29.74	14.87	38.58	16.07	38.19	14.55	34.59	14.70	34.11	14.34	38.70	12.88
RMSE	0.01	0.01	0.02	0.01	0.02	0.01	0.02	0.01	0.02	0.02	0.01	0.01
r	0.87	0.87	0.86	0.85	0.86	0.86	0.91	0.90	0.75	0.75	0.94	0.94
Slope	0.93	0.99	0.91	1.00	0.90	1.01	0.91	1.01	0.92	1.00	0.90	1.00

Table S2: New coefficients that resulted in the smallest cost function for each of the two algorithms evaluated, and for each satellite sensor. If interested in code used to derive coefficients, see data availability section for link to GitHub repository. Original coefficients can be found in [1]

	$K_d(490)^{NASA/ESA}$					$K_d(\lambda)^{QAA}$			
	A0	**A1**	**A2**	**A3**	**A4**	**A1**	**A2**	**A3**	**A4**
MODIS-Terra	-0.9688	-2.1177	2.4232	-3.3654	-1.5287	0.7589	0.9845	0.5973	11.5902
MODIS-Aqua	-1.0437	-0.1871	-7.8081	15.5137	-12.8250	2.7842	0.0000	-3.4312	-35.2503
VIIRS-SNPP	-0.9331	-1.6787	1.0895	-2.1979	-1.0046	0.1502	-0.8199	1.2391	-3.1546
VIIRS-JPSS	-0.7693	-2.2239	1.7810	-2.4596	-1.0182	3.0194	0.0000	-2.4206	-35.2523
OLCI-S3A	-0.9365	-1.6523	0.9479	-1.5629	0.0889	0.3224	0.6513	0.7598	4.0967
OLCI-S3B	-0.9633	-0.7257	0.7890	-4.1177	0.0561	-0.2756	-1.5233	1.6874	-3.1597
Global	N/A	N/A	N/A	N/A	N/A	2.6188	1.2322	1.2351	38.8292

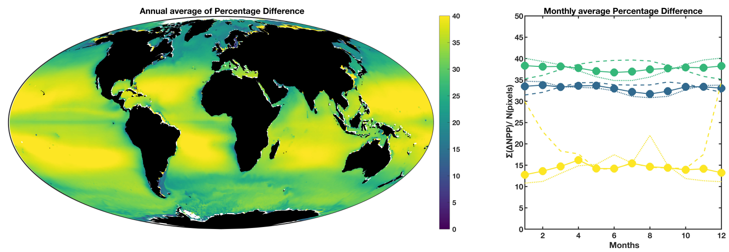

Figure 4: Difference in annual average $K_d(490)$ when using the original vs. the new coefficients as inputs.

Table S3: Statistical metrics of the distribution of $K_d(490)^{QAA}$ derived from monthly level-3 R_{rs} data for July 2020 for each sensor-pair. In the top part are the metrics for when using a single set of coefficients derived for Modis-Aqua available in Table S2 and in the bottom part are the metrics when using the individual coefficients derived for each specific sensor available in Table S2.

	Aqua vs. Terra	**Aqua vs. Viirs**	**Aqua vs. OLCI-S3A**	**Aqua vs. OLCI-S3B**	**Viirs vs. Terra**	**Viirs vs. OLCI S3A**	**Viirs vs. OLCI-S3B**	**Terra vs. OLCI-S3A**	**Terra vs. OLCI-S3B**	**OLCI S3A vs. OLCI S3B**
	Using 1 set of Modis-Aqua coefficients.									
Bias	1.004	0.859	0.876	0.886	1.170	1.023	1.035	0.876	0.886	1.010
ADP	6.692	17.965	16.440	15.402	19.107	9.226	9.093	15.761	14.737	6.704
RMSE	0.143	0.522	0.582	0.581	0.120	0.428	0.223	0.225	0.214	0.136
	Using the Individual sensor coefficients.									
Bias	1.063	1.039	0.866	0.981	1.037	0.833	0.956	0.813	0.929	1.141
ADP	12.761	9.437	17.446	13.419	9.685	21.523	12.194	26.254	9.737	18.197
RMSE	0.616	0.918	0.565	1.037	0.364	0.964	0.437	0.488	0.039	0.619

7 Author Contributions

"E. Boss and C. Begouen Demeaux conceived the idea. C. Begouen Demeaux performed the computations and analyzed the data. T. Westberry contributed to the interpretation of the NPP results and provided codes for the analysis. C. Begouen Demeaux wrote the first draft of the manuscript and all authors contributed to its revision."

8 Acknowledgments

The authors thank Marcel Babin for providing the COASTLOOC database. The authors thank all members of the BGC-Argo program without which this study would not have been possible. These data were collected and made freely available by the International Argo Program and the national programs that contribute to it (https://argo.ucsd.edu, https://www.ocean-ops.org). The Argo Program is part of the Global Ocean Observing System and data are accessible at https://doi.org/10.17882/42182. We thank Guillaume Bourdin and Nils Haentjens for coding help and advices.

Funding

This research was funded by NASA Ocean Biology and Biogeochemistry program grant number 80NSSC20M0203.

Conflicts of Interest

The authors declare that there is no conflict of interest regarding the publication of this article.

Data Availability

The matchup database between floats and Satellite-measured R_{rs} compiled by [1] was accessed from the Zenodo open access platform using the following doi: http://doi.org/10.5281/zenodo.7015427. Level-3 satellite images were accessed from https://oceancolor.gsfc.nasa.gov/l3/order/ and MLD model outputs were accessed from http://orca.science.oregonstate.edu/2160.by.4320.monthly.hdf.mld030.hycom.php. Once peer-review process is complete, all codes used to derive the new parametrization and to estimate NPP will be available on the Ocean Optics Github page (https://github.com/OceanOptics).

References

[1] C. Begouen Demeaux and E. Boss, "Validation of Remote-Sensing Algorithms for Diffuse Attenuation of Downward Irradiance Using BGC-Argo Floats," en, *Remote Sensing*, vol. 14, no. 18, p. 4500, 2022, ISSN: 2072-4292. DOI: 10.3390/rs14184500. [Online]. Available: https://www.mdpi.com/2072-4292/14/18/4500 (visited on 11/02/2022).

[2] C. Mobley, *The Oceanic Optics Book*, en. International Ocean Colour Coordinating Group, 2022, Medium: 924pp. Publisher: International Ocean Colour Coordinating Group (IOCCG). DOI: 10.25607/OBP-1710. [Online]. Available: https://repository.oceanbestpractices.org/handle/11329/1853 (visited on 11/01/2022).

[3] P. R. Oke *et al.*, "Evaluation of a near-global eddy-resolving ocean model," en, *Geoscientific Model Development*, vol. 6, no. 3, pp. 591–615, 2013, ISSN: 1991-9603. DOI: 10.5194/gmd-6-591-2013. [Online]. Available: https://gmd.copernicus.org/articles/6/591/2013/ (visited on 12/17/2022).

[4] T. Westberry, M. J. Behrenfeld, D. A. Siegel, and E. Boss, "Carbon-based primary productivity modeling with vertically resolved photoacclimation: CARBON-BASED PRODUCTION MODEL," en, *Global Biogeochemical Cycles*, vol. 22, no. 2, n/a–n/a, 2008, ISSN: 08866236. DOI: 10.1029/2007GB003078. [Online]. Available: http://doi.wiley.com/10.1029/2007GB003078 (visited on 11/02/2022).

[5] J. T. O. Kirk, *Light and Photosynthesis in Aquatic Ecosystems*, 3rd ed. Cambridge University Press, 2010.

[6] R. W. Austin and T. J. Petzold, "The Determination of the Diffuse Attenuation Coefficient of Sea Water Using the Coastal Zone Color Scanner," en, in *Oceanography from Space*, J. F. R. Gower, Ed., Boston, MA: Springer US, 1981, pp. 239–256. DOI: 10.1007/978-1-4613-3315-9_29. [Online]. Available: http://link.springer.com/10.1007/978-1-4613-3315-9_29 (visited on 11/02/2022).

[7] A. Morel, Y. Huot, B. Gentili, P. J. Werdell, S. B. Hooker, and B. A. Franz, "Examining the consistency of products derived from various ocean color sensors in open ocean (Case 1) waters in the perspective of a multi-sensor approach," en, *Remote Sensing of Environment*, vol. 111, no. 1, pp. 69–88, 2007, ISSN: 00344257. DOI: 10.1016/j.rse.2007.03.012. [Online]. Available: https://linkinghub.elsevier.com/retrieve/pii/S0034425707001307 (visited on 11/02/2022).

[8] C. Jamet, H. Loisel, and D. Dessailly, "Retrieval of the spectral diffuse attenuation coefficient in open and coastal ocean waters using a neural network inversion: RETRIEVAL OF DIFFUSE ATTENUATION," en, *Journal of Geophysical Research: Oceans*, vol. 117, no. C10, n/a–n/a, 2012, ISSN: 01480227. DOI: 10.1029/2012JC008076. [Online]. Available: http://doi.wiley.com/10.1029/2012JC008076 (visited on 11/02/2022).

[9] Z.-P. Lee, "Diffuse attenuation coefficient of downwelling irradiance: An evaluation of remote sensing methods," en, *Journal of Geophysical Research*, vol. 110, no. C2, p. C02017, 2005, ISSN: 0148-0227. DOI: 10.1029/2004JC002573. [Online]. Available: http://doi.wiley.com/10.1029/2004JC002573 (visited on 11/02/2022).

[10] Z. Lee *et al.*, "Penetration of UV-visible solar radiation in the global oceans: Insights from ocean color remote sensing: PENETRATION OF UV-VISIBLE SOLAR LIGHT," en, *Journal of Geophysical Research: Oceans*, vol. 118, no. 9, pp. 4241–4255, 2013, ISSN: 21699275. DOI: 10.1002/jgrc.20308. [Online]. Available: http://doi.wiley.com/10.1002/jgrc.20308 (visited on 11/02/2022).

[11] X. Xing, E. Boss, J. Zhang, and F. Chai, "Evaluation of Ocean Color Remote Sensing Algorithms for Diffuse Attenuation Coefficients and Optical Depths with Data Collected on BGC-Argo Floats," en, *Remote Sensing*, vol. 12, no. 15, p. 2367, 2020, ISSN: 2072-4292. DOI: 10.3390/rs12152367. [Online]. Available: https://www.mdpi.com/2072-4292/12/15/2367 (visited on 11/02/2022).

[12] Z. Lee, "Penetration of solar radiation in the upper ocean: A numerical model for oceanic and coastal waters," en, *Journal of Geophysical Research*, vol. 110, no. C9, p. C09019, 2005, ISSN: 0148-0227. DOI: 10.1029/2004JC002780. [Online]. Available: http://doi.wiley.com/10.1029/2004JC002780 (visited on 01/24/2023).

[13] X. Xing and E. Boss, "Chlorophyll-Based Model to Estimate Underwater Photosynthetically Available Radiation for Modeling, *In-Situ* , and Remote-Sensing Applications," en, *Geophysical Research Letters*, vol. 48, no. 7, Apr. 2021, ISSN: 0094-8276, 1944-8007. DOI: 10.1029/2020GL092189. [Online]. Available: https://onlinelibrary.wiley.com/doi/10.1029/2020GL092189 (visited on 02/03/2023).

[14] S. W. Bailey and P. J. Werdell, "A multi-sensor approach for the on-orbit validation of ocean color satellite data products," en, *Remote Sensing of Environment*, vol. 102, no. 1-2, pp. 12–23, 2006, ISSN: 00344257. DOI: 10.1016/j.rse.2006.01.015. [Online]. Available: https://linkinghub.elsevier.com/retrieve/pii/S0034425706000472 (visited on 12/12/2022).

[15] E. Organelli *et al.*, "A Novel Near-Real-Time Quality-Control Procedure for Radiometric Profiles Measured by Bio-Argo Floats: Protocols and Performances," en, *Journal of Atmospheric and Oceanic Technology*, vol. 33, no. 5, pp. 937–951, 2016, ISSN: 0739-0572, 1520-0426. DOI: 10.1175/JTECH-D-15-0193.1. [Online]. Available: https://journals.ametsoc.org/view/journals/atot/33/5/jtech-d-15-0193_1.xml (visited on 11/02/2022).

[16] A. R. Fay and G. A. McKinley, "Global open-ocean biomes: Mean and temporal variability," en, *Earth System Science Data*, vol. 6, no. 2, pp. 273–284, 2014, ISSN: 1866-3516. DOI: 10.5194/essd-6-273-2014. [Online]. Available: https://essd.copernicus.org/articles/6/273/2014/ (visited on 12/19/2022).

[17] Z.-P. Lee, Ed., *Remote sensing of inherent optical properties: Fundamentals, tests of algorithms, and applications.* 2006.

[18] Z. Lee, K. L. Carder, and R. A. Arnone, "Deriving inherent optical properties from water color: A multiband quasi-analytical algorithm for optically deep waters," en, *Applied Optics*, vol. 41, no. 27, p. 5755, Sep. 2002, ISSN: 0003-6935, 1539-4522. DOI: 10.1364/AO.41.005755. [Online]. Available: https://opg.optica.org/abstract.cfm?URI=ao-41-27-5755 (visited on 01/31/2023).

[19] R. M. Pope and E. S. Fry, "Absorption spectrum (380–700 nm) of pure water II Integrating cavity measurements," en, *Applied Optics*, vol. 36, no. 33, p. 8710, Nov. 1997, ISSN: 0003-6935, 1539-4522. DOI: 10.1364/AO.36.008710. [Online]. Available: https://opg.optica.org/abstract.cfm?URI=ao-36-33-8710 (visited on 02/09/2023).

[20] X. Zhang, L. Hu, and M.-X. He, "Scattering by pure seawater: Effect of salinity," en, *Optics Express*, vol. 17, no. 7, p. 5698, Mar. 2009, ISSN: 1094-4087. DOI: 10.1364/OE.17.005698. [Online]. Available: https://opg.optica.org/oe/abstract.cfm?uri=oe-17-7-5698 (visited on 02/09/2023).

[21] P. J. Werdell and S. W. Bailey, "An improved in-situ bio-optical data set for ocean color algorithm development and satellite data product validation," en, *Remote Sensing of Environment*, vol. 98, no. 1, pp. 122–140, 2005, ISSN: 00344257. DOI: 10.1016/j.rse.2005.07.001. [Online]. Available: https://linkinghub.elsevier.com/retrieve/pii/S0034425705002208 (visited on 12/19/2022).

[22] T. Zhang and F. Fell, "An empirical algorithm for determining the diffuse attenuation coefficient K_d in clear and turbid waters from spectral remote sensing reflectance: K$_{\mathrm{d}}$ in clear and turbid waters," en, *Limnology and Oceanography: Methods*, vol. 5, no. 12, pp. 457–462, Dec. 2007, ISSN: 15415856. DOI: 10.4319/lom.2007.5.457. [Online]. Available: http://doi.wiley.com/10.4319/lom.2007.5.457 (visited on 02/09/2023).

[23] M. J. Behrenfeld and P. G. Falkowski, "Photosynthetic rates derived from satellite-based chlorophyll concentration," en, *Limnology and Oceanography*, vol. 42, no. 1, pp. 1–20, 1997, ISSN: 00243590. DOI: 10.4319/lo.1997.42.1.0001. [Online]. Available: http://doi.wiley.com/10.4319/lo.1997.42.1.0001 (visited on 12/02/2022).

[24] M. J. Behrenfeld, E. Boss, D. A. Siegel, and D. M. Shea, "Carbon-based ocean productivity and phytoplankton physiology from space: PHYTOPLANKTON GROWTH RATES AND OCEAN PRODUCTIVITY," en, *Global Biogeochemical Cycles*, vol. 19, no. 1, 2005, ISSN: 08866236. DOI: 10.1029/2004GB002299. [Online]. Available: http://doi.wiley.com/10.1029/2004GB002299 (visited on 12/02/2022).

[25] T. P. Boyer *et al.*, *World ocean atlas 2018*, 2018. [Online]. Available: https://www.ncei.noaa.gov/archive/accession/NCEI-WOA18.

[26] M. S. Salama and W. Verhoef, "Two-stream remote sensing model for water quality mapping: 2SeaColor," en, *Remote Sensing of Environment*, vol. 157, pp. 111–122, 2015, ISSN: 00344257. DOI: 10.1016/j.rse.2014.07.022. [Online]. Available: https://linkinghub.elsevier.com/retrieve/pii/S0034425714002715 (visited on 12/17/2022).

[27] K. Alikas, S. Kratzer, A. Reinart, T. Kauer, and B. Paavel, "Robust remote sensing algorithms to derive the diffuse attenuation coefficient for lakes and coastal waters: Algorithm for diffuse attenuation coefficient," en, *Limnology and Oceanography: Methods*, vol. 13, no. 8, pp. 402–415, 2015, ISSN: 15415856. DOI: 10.1002/lom3.10033. [Online]. Available: https://onlinelibrary.wiley.com/doi/10.1002/lom3.10033 (visited on 12/17/2022).

[28] M. Stramska and P. Aniskiewicz, "Recent Large Scale Environmental Changes in the Mediterranean Sea and Their Potential Impacts on Posidonia Oceanica," en, *Remote Sensing*, vol. 11, no. 2, p. 110, 2019, ISSN: 2072-4292. DOI: 10.3390/rs11020110. [Online]. Available: http://www.mdpi.com/2072-4292/11/2/110 (visited on 12/17/2022).

[29] J. Marra and K. Heinemann, "Primary production in the North Pacific Central Gyre: Some new measurements based on c14," en, *Deep-Sea Research*, 1986.

[30] W. Balch, R. Evans, J. Brown, G. Feldman, C. McClain, and W. Esaias, "The remote sensing of ocean primary productivity: Use of a new data compilation to test satellite algorithms," en, *Journal of Geophysical Research*, vol. 97, no. C2, p. 2279, 1992, ISSN: 0148-0227. DOI: 10.1029/91JC02843. [Online]. Available: http://doi.wiley.com/10.1029/91JC02843 (visited on 12/17/2022).

[31] P. Lobanova, G. H. Tilstone, I. Bashmachnikov, and V. Brotas, "Accuracy Assessment of Primary Production Models with and without Photoinhibition Using Ocean-Colour Climate Change Initiative Data in the North East Atlantic Ocean," en, *Remote Sensing*, vol. 10, no. 7, p. 1116, 2018, ISSN: 2072-4292. DOI: 10.3390/rs10071116. [Online]. Available: http://www.mdpi.com/2072-4292/10/7/1116 (visited on 12/19/2022).

[32] A. Regaudie-de-Gioux *et al.*, "Multi-model remote sensing assessment of primary production in the subtropical gyres," en, *Journal of Marine Systems*, vol. 196, pp. 97–106, Aug. 2019, ISSN: 09247963. DOI: 10.1016/j.jmarsys.2019.03.007. [Online]. Available: https://linkinghub.elsevier.com/retrieve/pii/S0924796318303385 (visited on 01/03/2023).

[33] A. J. Irwin and M. J. Oliver, "Are ocean deserts getting larger?" en, *Geophysical Research Letters*, vol. 36, no. 18, p. L18609, Sep. 2009, ISSN: 0094-8276. DOI: 10.1029/2009GL039883. [Online]. Available: http://doi.wiley.com/10.1029/2009GL039883 (visited on 01/16/2023).

[34] S. R. Signorini, B. A. Franz, and C. R. McClain, “Chlorophyll variability in the oligotrophic gyres: Mechanisms, seasonality and trends,” en, *Frontiers in Marine Science*, vol. 2, 2015, ISSN: 2296-7745. DOI: 10.3389/fmars.2015.00001. [Online]. Available: http://journal.frontiersin.org/Article/10.3389/fmars.2015.00001/abstract (visited on 12/20/2022).